Momentum-Space Spin Antivortex and Spin Transport in Monolayer Pb

Kaijie Yang,[1] Yuanxi Wang [ORCID],[2,3] and Chao-Xing Liu[1,*]

[1]*Department of Physics, The Pennsylvania State University, University Park, Pennsylvania 16802, USA*
[2]*2-Dimensional Crystal Consortium, Materials Research Institute, The Pennsylvania State University, University Park, Pennsylvania 16802, USA*
[3]*Department of Physics, University of North Texas, Denton, Texas 76203, USA*

Nontrivial momentum-space spin texture of electrons can be induced by spin-orbit coupling and underpins various spin transport phenomena, such as current-induced spin polarization and the spin Hall effect. In this work, we find a nontrivial spin texture, spin antivortex, can appear at certain momenta on the $\Gamma - K$ line in a 2D monolayer Pb on top of SiC. Different from spin vortex due to the band degeneracy in the Rashba model, the existence of this spin antivortex is guaranteed by the Poincaré-Hopf theorem and thus topologically stable. Accompanied with this spin antivortex, a Lifshitz transition of Fermi surfaces occurs at certain momenta on the $K - M$ line, and both phenomena are originated from the anticrossing between the $j = 1/2$ and $j = 3/2$ bands. A rapid variation of the response coefficients for both the current-induced spin polarization and spin Hall conductivity is found when the Fermi energy is tuned around the spin antivortex. Our work demonstrates the monolayer Pb as a potentially appealing platform for spintronic applications.

Introduction.—Momentum-space spin textures of electronic bands often provide an intuitive picture to understand spin transport phenomena such as current-induced spin polarization (CISP, also known as the Edelstein effect or the inverse spin galvanic effect) [1–7] and spin Hall effect (SHE) [8–10] in spin-orbit coupled materials. The Rashba model [11–14], for example, possesses a spin texture of the vortex type, for which electron spins are oriented tangentially along the Fermi contour and form a vortex texture (also called helical texture) for each of the two spin-split bands. Under an electric field, the nonequilibrium distribution of electrons around a shifted Fermi contour carrying spin vortices leads to a net CISP. Such analytical models of spin vortices usually capture spin textures around high-symmetry k points but can be insufficient in describing response functions that rely on *integrals* over the entire Brillouin zone (BZ) in realistic materials, where complex spin textures arising far from high-symmetry k points contribute dominantly. Here we introduce a new type of spin texture, a *spin antivortex*, with a unique movable, but unremovable nature in the momentum space.

We demonstrate that spin antivortices can be hosted by atomically thin metals with strong spin orbit coupling (SOC). Such 2D metals have been realized using the confinement heteroepitaxy technique [15], where metal species intercalate underneath graphene epitaxially grown on an insulating SiC substrate. This new growth technique can produce air-stable, crystalline 2D metals at scale, with extraordinary optical [16] and transport properties [15] that may enable the development of new device applications of

2D materials [17–19]. In particular, the strong SOC in 2D heavy metals, such as Pb, Pt, Sn, Au, and Bi, can naturally produce spin-split bands when combined with the inversion symmetry breaking guaranteed by the graphene-metal-SiC architecture.

In this work, we study the spin texture for the 2D Pb monolayer and find that besides the spin vortices around high-symmetry momenta Γ, M, and K, spin antivortices with the opposite winding numbers exist at non-high-symmetry momenta along the $\Gamma - K$ lines, as labeled by six red crosses in Fig. 1(a). Unlike the Rashba model, in which spin vortices are induced by band degeneracy, the spin antivortices in this system are guaranteed by the Poincaré-Hopf theorem, and thus reveal a movable but locally unremovable nature. A Lifshitz transition of the Fermi surface along $K - M$ accompanies the emergence of spin antivortices in a similar energy range. To quantitatively predict the spectroscopic signatures of the spin anti-vortices and Lifshitz transition, we model their effect on spin transport by combining density functional theory (DFT) [20–25] with the Green's function formalism to show that they induce a rapid change of CISP and SHE when the Fermi energy is tuned to align with them. The effect of short-range disorder scattering is also discussed by including the vertex correction in the Green's function formalism. Our work will guide experimental studies on spin phenomena and pave the way to the spintronic applications of 2D heavy metals.

Lifshitz transition and momentum-space spin antivortex in monolayer Pb.—We start from the ground state lattice structure and electronic structure of monolayer Pb on top of
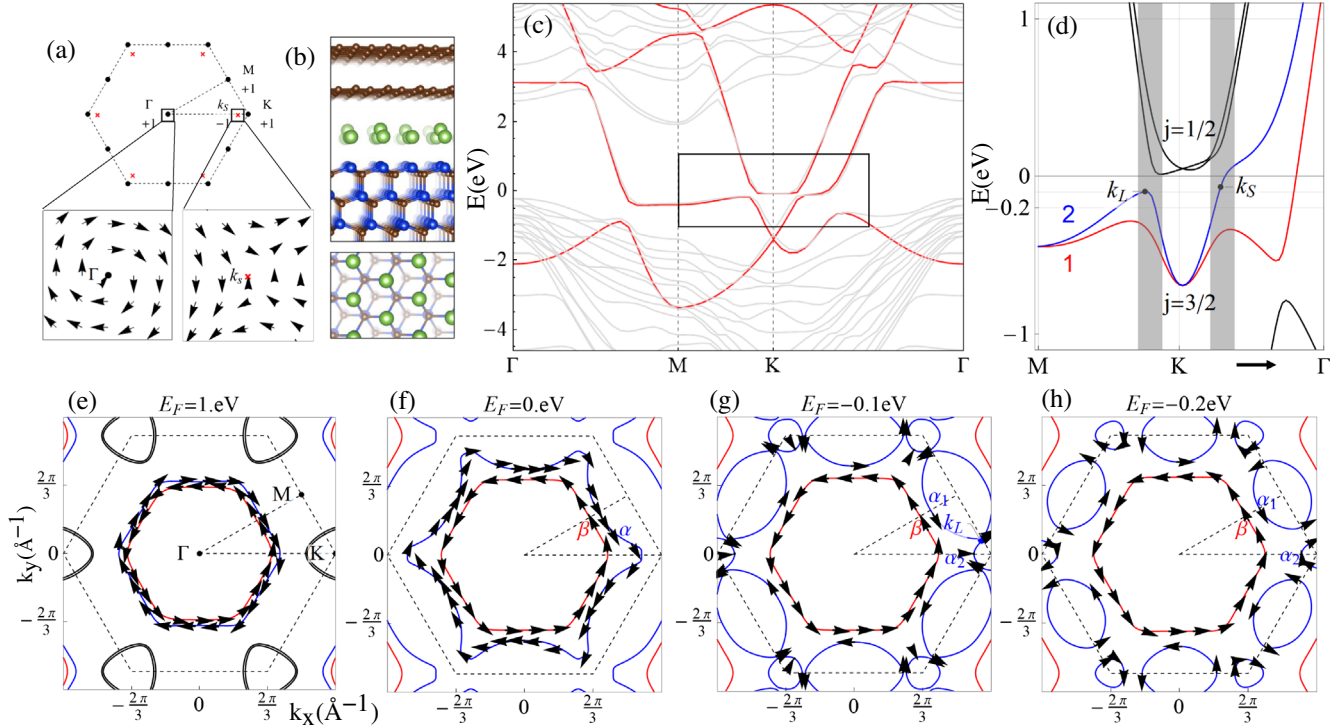
FIG. 1. (a) The locations of spin vortices (black dots) and antivortices (red crosses) in the first BZ and the spin texture for the spin vortex around the Γ point with a winding number $+1$ and the antivortex around the k_S point with a winding number -1. (b) The lattice structure of the intercalated monolayer Pb between SiC substrate and graphene. (c) The electronic band structure without SOC from first principal calculation (gray lines) and from the maximal localized Wannier function (MLWF) (red lines). (d) The band spectrum from MLWF with SOC for the energy range of the black box in (b). The gray region is the anticrossing regime of $j = 1/2$ and $j = 3/2$ bands. k_L and k_S label the locations of the Lifshitz transition point and spin antivortex. (e)–(h) Fermi surfaces and spin texture of band 1 and 2 for $E_F = 1.0, 0.0, -0.1, -0.2$ eV. $\alpha(\beta)$ are hole pockets for band 1(2) around Γ before the Lifshitz transition. Black lines are electron Fermi pockets. $\alpha_1(\alpha_2)$ are Fermi surface pockets for band 2 around $M(K)$ after Lifshitz transition.

the SiC substrate. The Pb atoms form a triangular lattice described by the C_{3v} symmetry group that can be generated by a threefold rotation and an in-plane mirror. Inversion symmetry is broken due to the local environment, as shown in Fig. 1(b). The electronic structure of this system at the DFT level (see Supplemental Material [26] Sec. I. B for details) without and with SOC are, respectively, shown in Figs. 1(c) and 1(d). Focusing on the -1 to 1 eV energy range near the Fermi energy, the two strongly dispersive bands are mainly characterized by Pb p_x and p_y orbitals; the other weakly dispersive band anticrossing with the p_x and p_y bands is of p_z orbital character from both Pb and the topmost Si layer of the SiC substrate. Band interpolation using maximally localized Wannier functions was then performed using the above four orbitals for initial projections (details in Supplemental Material [26]). The resulting Wannier-interpolated bands in Fig. 1(c) agrees well with the original DFT ones within the manifold of the four orbitals. After introducing atomic SOC to the tight binding Hamiltonian obtained from Wannierization, we obtain low-energy bands shown in Fig. 1(d). Labeling bands with SOC by total angular momenta j at K, the $j = 1/2$ bands are mainly dominated by Si p_z orbitals and the $j = 3/2$ bands

[labeled as bands 1 and 2 in Fig. 1(d)] come from Pb $p_x p_y$ orbitals; these two bands anticross around K for $E_F = -0.1$ eV.

We next show the evolution of Fermi surfaces across a Lifshitz transition in Figs. 1(e)–1(h), where E_F is lowered from 1.0 eV to 0.0, -0.1 and -0.2 eV. At $E_F = 1.0$ eV, the spin-split hole pockets α (blue) and β (red) and the spin-split electron pockets around K (black) come from Pb p_x, p_y orbitals. As the Fermi energy lowers to $E_F = 0.0$ eV, the electron pockets shrink and disappear, while the hole pockets extend towards the BZ boundary. As the Fermi energy decreases further, the hole pocket α is split into the electron pockets α_1 and α_2 around the M and K points, as shown in Fig. 1(h). A Lifshitz transition that changes the Fermi surface topology occurs at the momentum k_L along the $K - M$ line at $E_F = -0.1$ eV, as shown in Fig. 1(g).

Also evolving with lowering Fermi energies along Figs. 1(e)–1(h) are spin textures of the Fermi pockets. At $E_F = 1.0$ eV, the spin textures of two hole pockets are of Rashba-type. As the Fermi energy lowers, the spin texture of the inner hole pocket β (red) remains the same while dramatic changes occur for the outer hole pocket α (blue) that experiences the Lifshitz transition.
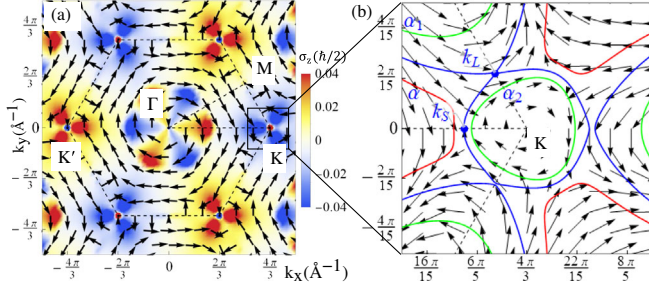
FIG. 2. (a) Spin texture of the band 2 in the whole BZ. The arrows depict in-plane spin polarization while the background color reveals the z-component spin polarization. The spin vortices with winding number $+1$ exist at high symmetry points Γ, M, K, K'. (b) The zoom-in of spin texture around K. A spin antivortex shows up on the $\Gamma - K$ line at the k_S point on Fermi surfaces around $E_F = -0.1$ eV, concurrent with the Lifshitz transition. The red, blue, green lines are Fermi surfaces of $E_F = 0.0, -0.1, -0.2$ eV, respectively.

By comparing the spin direction of the blue Fermi pocket at $E_F = 0.0$ and $E_F = -0.2$ eV, one notices that the spin direction of the Fermi pocket α_1 around M at $E_F = -0.2$ eV follows that at $E_F = 0.0$ eV, while the spin direction of the Fermi pocket α_2 around K at $E_F = -0.2$ eV reverses its sign, as compared to that at $E_F = 0.0$ eV. To see this feature more clearly, we focus on the spin texture of band 2 in the whole BZ, as shown in Fig. 2(a), in which the arrows show the in-plane spin directions and the colors indicate the z-component spin. It is clear that the in-plane spin forms vortices around Γ, M, K, and K'. Zooming in on the spin texture of band 2 around K in Fig. 2(b), we find that, besides the vortex around K, another antivortex centered at k_S appears along the $\Gamma - K$ line. The lines α, α_1, and α_2 in Fig. 2(b) show the Fermi surfaces at $E_F = 0.0$ and $E_F = -0.2$ eV, respectively, and we indeed see a sign change of the spin direction for the momenta at the left and right sides of k_S along the $\Gamma - K$ line between these two Fermi surfaces, consistent with the Fermi pocket plot in Figs. 1(f) and 1(h).

The existence of the spin antivortex can be viewed as a consequence of the Poincaré-Hopf theorem of a tangential vector field on a compact manifold [40]. The BZ is a torus and we only focus on the in-plane spin component, which can be regarded as a tangential field. According to the Poincaré-Hopf theorem, the total of winding numbers around spin vortices is the Euler number of the torus, namely, zero. The winding numbers of spin vortices at six high symmetry momenta, namely, Γ, K, K' and three M points, are all $+1$, as shown in Fig. 2(a). On the other hand, there are six antivortices due to the combination of C_3 and time reversal $\mathcal{T}$ symmetries, each with winding number -1, as shown in Fig. 1(a). Thus, the total winding number in the whole BZ vanishes, as required by the Poincaré-Hopf theorem. This analysis suggests that, unlike a spin vortex around high symmetry momenta, each spin antivortex is

movable along the $\Gamma - K$ lines, but is locally stable due to its topological nature. The difference between spin antivortex and other spin texture, such as spin vortex in the Rashba model, is further discussed in Sec. II. C of Supplemental Material [26]. In addition, it is shown that the location of spin antivortex can be controlled by an external gate voltage, as discussed in Sec. II. B of Supplemental Material [26].

It is interesting to notice that both the Lifshitz transition and the spin antivortex occur approximately around $E_F \approx -0.1$ eV, as shown in Fig. 2(b). This is because both phenomena are related to the anticrossings between the $j = 1/2$ bands from p_z orbitals and the $j = 3/2$ bands from $p_{x,y}$ orbitals around K or K', as shown by the gray regime in Fig. 1(d). We provide more detailed analysis on how the band anticrossing can induce the Lifshitz transition and spin antivortex in the Supplemental Material [26] Sec. II. B.

Current-induced spin polarization and the spin Hall effect.—The Lifshitz transition and spin antivortex can be experimentally verified by their spectroscopic signatures: they can, in principle, be extracted through the spin-resolved angular-resolved photoemission spectroscopy [41]. Here we focus on the spin transport phenomena of CISP and SHE, which are described by the response equations, $S_k = \sum_i \chi_{ki} E_i$ for CISP and $J_j^k = \sum_i \sigma_{ji}^k E_i$ for SHE, respectively. Here S_k is the spin operator with $k = x, y, z$, v_j is the velocity operator with $i, j = x, y$ and $J_j^k = \{S_k, v_j\}/2$ is the spin current operator. Based on the threefold rotation and in-plane mirror symmetries, the nonzero in-plane current response coefficients for the x-direction electrical field are χ_{yx} for CISP and $\sigma_{yx}^z, \sigma_{xx}^x = -\sigma_{yx}^y$ for SHE from the Neumann's principles [42].

The detailed form of the response coefficients χ_{ij} and σ_{ji}^k can be derived from the standard linear response theory and are given by

$$\chi_{ij}(E_F) = \int \frac{d^2\mathbf{k}}{(2\pi)^2} \chi_{ij}(\mathbf{k}, E_F)$$
$$= -\frac{1}{2\pi} \int \frac{d^2\mathbf{k}}{(2\pi)^2} \mathrm{Tr} S_i G^R(\mathbf{k}, E_F) \Gamma_j(\mathbf{k}) G^A(\mathbf{k}, E_F) \quad (1)$$

and

$$\sigma_{ij}^k(E_F) = \int \frac{d^2\mathbf{k}}{(2\pi)^2} \sigma_{ij}^k(\mathbf{k}, E_F)$$
$$= -\frac{1}{2\pi} \int \frac{d^2\mathbf{k}}{(2\pi)^2} \mathrm{Tr} J_i^k(\mathbf{k}) G^R(\mathbf{k}, E_F) \Gamma_j(\mathbf{k}) G^A(\mathbf{k}, E_F),$$
$$(2)$$

where G^R and G^A are the retarded and advanced Green's functions, Tr is the trace taken over band indices, and the vertex operator $\Gamma_j(\mathbf{k})$ is defined as $\Gamma_j(\mathbf{k}, E) = J_j(\mathbf{k}) + \gamma_j(E)$ with the current operator $J_j = -ev_j$ and
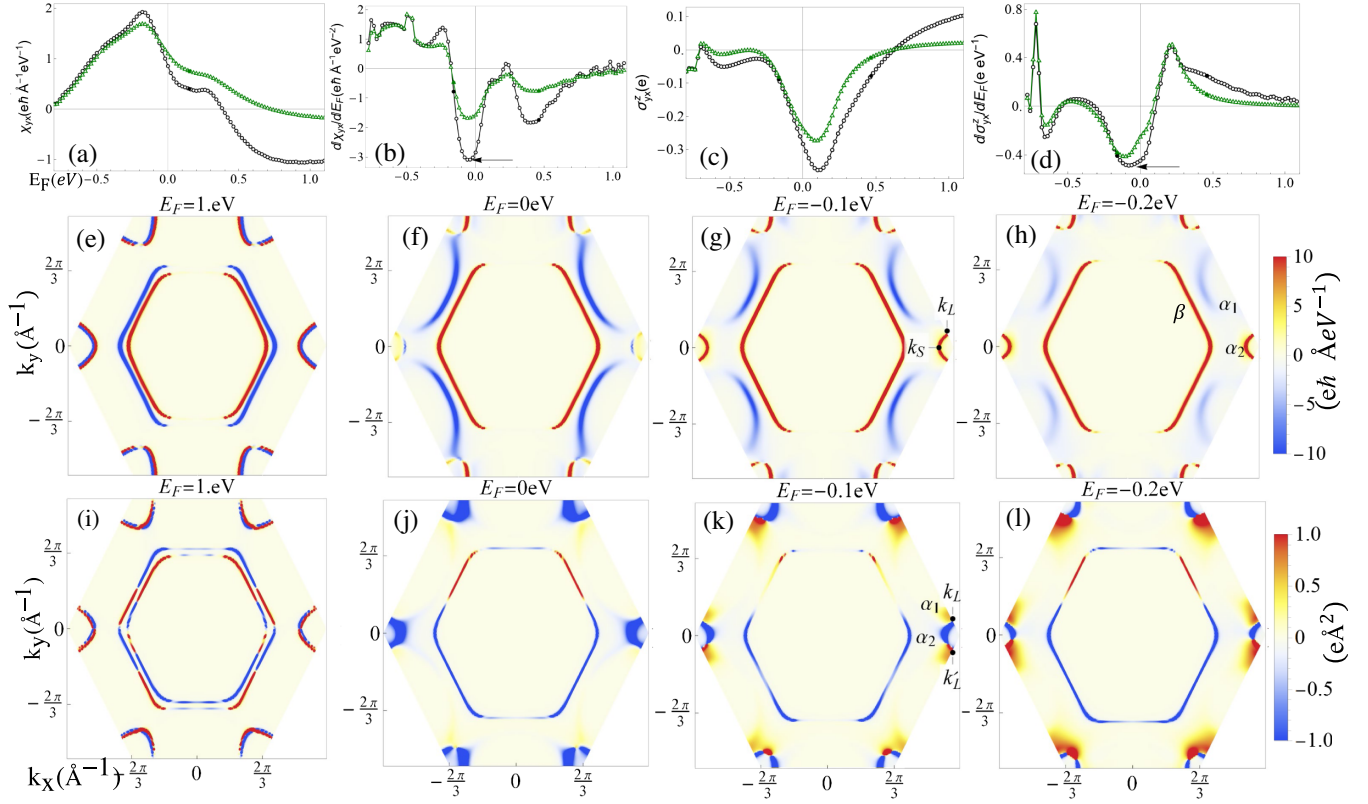
FIG. 3. (a),(b),(c), and (d) show χ_{yx}, $d\chi_{yx}/dE_F$, σ_{yx}^z, and $d\sigma_{yx}^z/dE_F$, respectively, as a function of E_F, in the clean case (black lines with circles) and with disorder scattering (green lines with triangles) for different E_F. (e)–(h) and (i)–(l) show the momentum resolved contribution $\chi_{ij}(\boldsymbol{k}, E_F)$ to the CISP and $\sigma_{ij}^k(\boldsymbol{k}, E_F)$ to the SHE, respectively, over the BZ for $E_F = 1.0, 0.0, -0.1, -0.2$ eV (without vertex correction).

$$\gamma_j(E) = n_i V_0^2 \int \frac{d^2\boldsymbol{l}}{(2\pi)^2} G^R(\boldsymbol{l}, E)[J_j(\boldsymbol{l}, E) + \gamma_j(E)]G^A(\boldsymbol{l}, E).$$

(3)

Here, γ_j describes the vertex correction to the current operator from the ladder diagram of disorder scattering with the disorder density n_i and scattering strength V_0 [43]. We apply the linear response formalism to the above-mentioned tight-binding model parametrized using Wannier functions; details of the numerical technique are discussed in the Supplemental Material [26] Sec. I.

Figure 3 summarizes our main numerical results for $\chi_{yx}(E_F)$ for CISP and $\sigma_{yx}^z(E_F)$ for SHE, respectively. Here the green line is for the case without the vertex correction, namely, $\Gamma_j(\boldsymbol{k}, E) = J_j(\boldsymbol{k})$, and the black line with vertex correction. We first analyze $\chi_{yx}(E_F)$ and plot its momentum resolved contribution $\chi_{yx}(\boldsymbol{k}, E_F)$ of Eq. (1) in Figs. 3(e)–3(h). We find that the main contribution to CISP comes from the Fermi surface since $G^R(\boldsymbol{k}, E_F)G^A(\boldsymbol{k}, E_F)$ in Eq. (1) can be approximated by $\delta(E_F - \epsilon_{nk})$ in the dilute disorder limit. At $E_F = 1.0$ eV, due to the opposite spin texture for the two hole pockets, they contribute oppositely to CISP, as shown in Fig. 3(e). The outer Fermi pocket will be dominant and

thus gives rise to the negative sign of χ_{yx}, resembling the CISP contribution in the standard Rashba model [11]. Near the Lifshitz transition, a dramatic change occurs to the outer Fermi pocket α_2 around K and K'. When lowering the Fermi energy from $E_F = 0.0$ to -0.1 eV, one can clearly see that the Fermi pocket α_2 around K and K' varies from blue (negative) to red (positive), as shown in Figs. 3(f) and 3(g). Physically, this sign change directly reflects the presence of spin antivortices, as the spin direction on the Fermi pocket α_2 around K and K' changes its sign across the spin antivortex. In addition, the contribution to CISP from the Fermi pocket α_1 around M also decreases due to the reduction of relaxation time (See Sec. II. C of Supplemental Material [26]). Combining the above factors leads to (i) the positive sign of χ_{yx} in this Fermi energy range ($E_F < 0.3$ eV) and (ii) a rapid increase of χ_{yx} around $E_F \approx -0.1$ eV as E_F decreases. To see this rapid change more clearly, we take a derivative of χ_{yx} with respect to E_F, as shown in Fig. 3(b). The peak in the amplitude of $d\chi_{yx}/dE_F$ indeed occurs around $E_F \approx -0.1$ eV, as shown by the arrow in Fig. 3(b), and thus is induced by the Fermi surface crossing the antivortex. The SHE also reveals a rapid change around $E_F \approx -0.1$ eV, as shown by a similar peak appears for $d\sigma_{yx}^z/dE_F$ in Fig. 3(d). This is because the

contribution to SHE around the Fermi pockets α_1 close to the Lifshitz transition point k_L and that around α_2 close to k'_L abruptly changes sign from negative (blue) to positive (red) when lowering the Fermi energy from $E_F = 0.0$ to -0.1 eV, as shown in Figs. 3(j) and 3(k). Detailed analysis suggests that the sign change of contribution around k_L and k'_L is more closely related to the Lifshitz transition due to the fact that the SHE mainly is contributed from interband matrix elements rather than the intraband Fermi surface contribution, as discussed in Sec. II. D of the Supplemental Material [26]. The influence of disorder scattering is also evaluated through the vertex correction, as shown by the dashed lines in Figs. 3(a)–3(d). We generally find both the values of χ_{yx} and σ_{yx}^z, as well as $d\chi_{yx}/dE_F$ and $d\sigma_{yx}^z/dE_F$, around $E_F = 1.0$ eV are enhanced by disorder scattering, as discussed in details in Secs. II. C and II. D of Supplemental Material [26].

Conclusion and discussion.—In conclusion, the spin antivortices and Lifshitz transition induced by the anticrossing between the p_z and $p_{x,y}$ bands strongly affect spin transport phenomena in the monolayer Pb on SiC. By choosing appropriate parameters (see Sec. II. E of the Supplemental Material [26]), we find σ_{yx}^z is of the order $10^{-1}e$ in our model and the corresponding spin Hall angle is $\sim 10^{-2}$, comparable to the existing experimentally measured values [44–46]. Based on the same values, we find the variation of σ_{yx}^z across the band anticrossing regime is around $\sim 0.3e$, and thus should be measurable by tuning the carrier density of 2D Pb in experiments. For CISP, $\chi_{yx}/\hbar$ is of the order 10^{-8} nm^{-2} V^{-1} m and its variation is $\sim 2 \times 10^{-8}$ nm^{-2} V^{-1} m in the band anticrossing regime. The charge-to-spin conversion efficiency $2ev_f\chi_{yx}/\hbar\sigma_{xx}$ is ~ 0.1, where v_f is the Fermi velocity and σ_{xx} is the longitudinal conductivity. This efficiency is close to that proposed and measured of graphene on a transition-metal dichalcogenide [47,48]. While Pb films have been grown on top of SiC with different growth methods [49–53], our theory suggests the monolayer Pb as an excellent platform for the study of spin transport phenomena and spintronic applications.

*cxl56@psu.edu

[1] V. M. Edelstein, Solid State Commun. **73**, 233 (1990).
[2] Y. K. Kato, R. C. Myers, A. C. Gossard, and D. D. Awschalom, Phys. Rev. Lett. **93**, 176601 (2004).
[3] A. Y. Silov, P. Blajnov, J. Wolter, R. Hey, K. Ploog, and N. Averkiev, Appl. Phys. Lett. **85**, 5929 (2004).
[4] V. Sih, R. Myers, Y. Kato, W. Lau, A. Gossard, and D. Awschalom, Nat. Phys. **1**, 31 (2005).
[5] H. J. Zhang, S. Yamamoto, B. Gu, H. Li, M. Maekawa, Y. Fukaya, and A. Kawasuso, Phys. Rev. Lett. **114**, 166602 (2015).
[6] C. H. Li, O. M. van't Erve, S. Rajput, L. Li, and B. T. Jonker, Nat. Commun. **7**, 1 (2016).
[7] I. Žutić, J. Fabian, and S. D. Sarma, Rev. Mod. Phys. **76**, 323 (2004).
[8] J. E. Hirsch, Phys. Rev. Lett. **83**, 1834 (1999).
[9] J. Sinova, D. Culcer, Q. Niu, N. A. Sinitsyn, T. Jungwirth, and A. H. MacDonald, Phys. Rev. Lett. **92**, 126603 (2004).
[10] S. Murakami, N. Nagaosa, and S.-C. Zhang, Science **301**, 1348 (2003).
[11] J.-I. Inoue, G. E. W. Bauer, and L. W. Molenkamp, Phys. Rev. B **67**, 033104 (2003).
[12] M. Trushin and J. Schliemann, Phys. Rev. B **75**, 155323 (2007).
[13] A. Johansson, J. Henk, and I. Mertig, Phys. Rev. B **93**, 195440 (2016).
[14] J.-I. Inoue, G. E. W. Bauer, and L. W. Molenkamp, Phys. Rev. B **70**, 041303(R) (2004).
[15] N. Briggs, B. Bersch, Y. Wang, J. Jiang, R. J. Koch, N. Nayir, K. Wang, M. Kolmer, W. Ko, A. D. L. F. Duran *et al.*, Nat. Mater. **19**, 637 (2020).
[16] M. A. Steves, Y. Wang, N. Briggs, T. Zhao, H. El-Sherif, B. M. Bersch, S. Subramanian, C. Dong, T. Bowen, A. D. L. Fuente Duran *et al.*, Nano Lett. **20**, 8312 (2020).
[17] P. Miró, M. Audiffred, and T. Heine, Chem. Soc. Rev. **43**, 6537 (2014).
[18] A. Avsar, H. Ochoa, F. Guinea, B. Özyilmaz, B. J. Van Wees, and I. J. Vera-Marun, Rev. Mod. Phys. **92**, 021003 (2020).
[19] S. Das, J. A. Robinson, M. Dubey, H. Terrones, and M. Terrones, Annu. Rev. Mater. Res. **45**, 1 (2015).
[20] G. Y. Guo, Y. Yao, and Q. Niu, Phys. Rev. Lett. **94**, 226601 (2005).
[21] G.-Y. Guo, S. Murakami, T.-W. Chen, and N. Nagaosa, Phys. Rev. Lett. **100**, 096401 (2008).
[22] F. Freimuth, S. Blügel, and Y. Mokrousov, Phys. Rev. Lett. **105**, 246602 (2010).
[23] S. Lowitzer, M. Gradhand, D. Ködderitzsch, D. V. Fedorov, I. Mertig, and H. Ebert, Phys. Rev. Lett. **106**, 056601 (2011).
[24] M. Gradhand, D. V. Fedorov, P. Zahn, and I. Mertig, Phys. Rev. Lett. **104**, 186403 (2010).
[25] M. Gradhand, D. V. Fedorov, P. Zahn, and I. Mertig, Phys. Rev. B **81**, 245109 (2010).
[26] See Supplemental Material at http://link.aps.org/supplemental/10.1103/PhysRevLett.128.166601 for construction of the tight binding model from DFT and detailed numerical calculation of spin transport response functions for Rashba 2DEG and 2D Pb, which includes Refs. [27–39].
[27] J. P. Perdew, K. Burke, and M. Ernzerhof, Phys. Rev. Lett. **77**, 3865 (1996).
[28] J. P. Perdew, K. Burke, and M. Ernzerhof, Phys. Rev. Lett. **78**, 1396(E) (1997).
[29] P. E. Blöchl, Phys. Rev. B **50**, 17953 (1994).
[30] G. Kresse and D. Joubert, Phys. Rev. B **59**, 1758 (1999).

[31] G. Kresse and J. Furthmüller, Phys. Rev. B **54**, 11169 (1996).

[32] S. Grimme, J. Antony, S. Ehrlich, and H. Krieg, J. Chem. Phys. **132**, 154104 (2010).

[33] P. Giannozzi, S. Baroni, N. Bonini, M. Calandra, R. Car, C. Cavazzoni, D. Ceresoli, G. L. Chiarotti, M. Cococcioni, I. Dabo *et al.*, J. Phys. Condens. Matter **21**, 395502 (2009).

[34] N. Marzari and D. Vanderbilt, Phys. Rev. B **56**, 12847 (1997).

[35] A. A. Mostofi, J. R. Yates, Y.-S. Lee, I. Souza, D. Vanderbilt, and N. Marzari, Comput. Phys. Commun. **178**, 685 (2008).

[36] I. Souza, N. Marzari, and D. Vanderbilt, Phys. Rev. B **65**, 035109 (2001).

[37] Y.-W. Wei, C.-K. Li, Y. Cao, and J. Feng, Comput. Phys. Commun. **258**, 107551 (2021).

[38] J. C. A. Barata and M. S. Hussein, Braz. J. Phys. **42**, 146 (2012).

[39] J. Sinova, S. O. Valenzuela, J. Wunderlich, C. H. Back, and T. Jungwirth, Rev. Mod. Phys. **87**, 1213 (2015).

[40] W. Fulton, *Algebraic Topology: A First Course* (Springer Science & Business Media, New York, 2013), Vol. 153.

[41] J. A. Sobota, Y. He, and Z.-X. Shen, Rev. Mod. Phys. **93**, 025006 (2021).

[42] F. E. Neumann and O. E. Meyer, *Vorlesungen über die Theorie der Elasticität der festen Körper und des Lichtäthers, gehalten an der Universität Königsberg* (B.G. Teubner, Leipzig, 1885).

[43] G. D. Mahan, *Many-Particle Physics* (Springer Science & Business Media, New York, 2013).

[44] M. Morota, Y. Niimi, K. Ohnishi, D. H. Wei, T. Tanaka, H. Kontani, T. Kimura, and Y. Otani, Phys. Rev. B **83**, 174405 (2011).

[45] O. Mosendz, V. Vlaminck, J. E. Pearson, F. Y. Fradin, G. E. W. Bauer, S. D. Bader, and A. Hoffmann, Phys. Rev. B **82**, 214403 (2010).

[46] K. Ando and E. Saitoh, J. Appl. Phys. **108**, 113925 (2010).

[47] T. S. Ghiasi, A. A. Kaverzin, P. J. Blah, and B. J. van Wees, Nano Lett. **19**, 5959 (2019).

[48] M. Offidani, M. Milletarì, R. Raimondi, and A. Ferreira, Phys. Rev. Lett. **119**, 196801 (2017).

[49] A. Yurtsever, J. Onoda, T. Iimori, K. Niki, T. Miyamachi, M. Abe, S. Mizuno, S. Tanaka, F. Komori, and Y. Sugimoto, Small **12**, 3956 (2016).

[50] S. Chen, P. A. Thiel, E. Conrad, and M. C. Tringides, Phys. Rev. Mater. **4**, 124005 (2020).

[51] J. Wang, M. Kim, L. Chen, K.-M. Ho, M. Tringides, C.-Z. Wang, and S. Wang, Phys. Rev. B **103**, 085403 (2021).

[52] M. Hupalo, X. Liu, C.-Z. Wang, W.-C. Lu, Y.-X. Yao, K.-M. Ho, and M. C. Tringides, Adv. Mater. **23**, 2082 (2011).

[53] X. Liu, T. Hu, Y. Miao, D. Ma, P. K. Chu, F. Ma, and K. Xu, J. Appl. Phys. **117**, 065304 (2015).